Computational Materials Science 150 (2018) 369–380

Contents lists available at ScienceDirect

Computational Materials Science

journal homepage: www.elsevier.com/locate/commatsci

Heat and fluid flow in additive manufacturing – Part II: Powder bed fusion of stainless steel, and titanium, nickel and aluminum base alloys

T. Mukherjee[a], H.L. Wei[a], A. De[b], T. DebRoy[a,*]

[a] Department of Materials Science and Engineering, The Pennsylvania State University, University Park, PA 16802, USA
[b] Department of Mechanical Engineering, Indian Institute of Technology, Bombay 400076, India

ARTICLE INFO

Keywords:
Powder bed fusion
Additive manufacturing
Heat and fluid flow
Lack of fusion defect
Distortion

ABSTRACT

The most important metallurgical variables that affect the structure and properties of components produced by powder bed fusion (PBF) are examined using a model, proposed and validated in part-I of this paper. These variables include the temperature and velocity fields, build shape and size, cooling rates, solidification parameters, dendrite arm spacing, hardness, distortion and lack of fusion defects for four common alloys used in additive manufacturing (AM), stainless steel 316 (SS 316), Ti-6Al-4V, Inconel 718 and AlSi10Mg. The process parameters examined include laser power, scanning speed, powder layer thickness, packing efficiency and hatch spacing. Among the four alloys, the largest molten pool of AlSi10Mg ensures good fusional bonding among layers and hatches but exhibits high solidification shrinkage. Therefore, AlSi10Mg is the most susceptible to distortion among the four alloys. SS 316 exhibits the opposite trend because of its smallest molten pool among the four alloys. For a particular alloy, lack of fusion and distortion can be minimized by careful selection of hatch spacing and scanning speed. For the dendritic growth of SS 316 and AlSi10Mg, refinement of the solidification microstructure through close spacing of the dendrite arms can be achieved using thinner layers and faster scanning. Asymmetry in liquid pool geometry because of the difference in the thermal properties of powder bed and solidified build can be minimized by reducing the scanning speed.

1. Introduction

In laser-assisted powder bed fusion (PBF), alloy powders are added progressively in thin layers and melted using a laser beam. After solidification, the molten alloy takes the shape and size of the desired component [1]. Several complex physical processes take place during PBF. Absorption of the laser beam by the powder bed, melting of a region below the beam and its solidification occur rapidly. Inside the liquid pool, the metal circulates at fairly high velocities driven by the spatial gradient of surface tension and buoyancy force. Heat transfer affects the temperature field, local cooling rates, build shape and size and the extent of fusion between adjacent layers and hatches [1]. The complexity of the thermal cycles in a multi-layer, multi-hatch, component results in spatial variation of the microstructure and anisotropy of mechanical properties of the component. Rapid heating, cooling and solidification of the molten pool also make the components susceptible to distortion [1–3]. All these features must be taken into account for improved understanding of the laser assisted PBF process.

Several attempts have been made to model the heat transfer and fluid flow in PBF-AM process. Finite element based heat conduction models [4–9] are used to calculate 3D transient temperature distribution [4,5,8,9], build geometry [5,8], cooling rate, cell spacing, solidification morphology [4,5,8] and surface roughness [7]. However, these models ignore the effect of convective transport of heat inside the molten pool which is the main mechanism of heat transfer within the molten pool [1]. Therefore, the calculated temperature values and cooling rates are significantly overestimated [1]. In some investigations, the effects of liquid metal flow have been considered to calculate temperature distribution [10], build geometry [10–12], solidification morphology [10,13], microstructure evolution [14] and surface defects [15]. However, these calculations are often done for a single track [10–14] and unable to explain the causes of anisotropy and spatial non-uniformity of structure and properties observed in multi-layer, multi-hatch, builds. Thermo-physical properties are often assumed to be independent of temperature, powder size and packing efficiency [15] for simplicity. Powder scale models [16–22] consider convective flow of molten metal and properties that depend on temperature, powder size and packing efficiency and are applicable for multi-layer, multi-hatch, components. They are used to predict residual stresses [16], build geometry [16–19], lack of fusion defects [20–22] and spatter formation

* Corresponding author.
E-mail address: debroy@psu.edu (T. DebRoy).

https://doi.org/10.1016/j.commatsci.2018.04.027
Received 17 February 2018; Received in revised form 10 April 2018; Accepted 11 April 2018

[22]. However, they are often applied in 2D [19] and are computationally intensive [16,17]. Two-dimensional models are not suitable for calculating important metallurgical variables such as, cooling rates, solidification parameters and grain structure. Transport phenomena based mathematical frameworks provide an improved understanding of PBF process. What is needed and currently not available is a rigorously tested and computationally efficient numerical framework that considers the effects of molten metal convection and accurate thermo-physical properties of powder bed. Such models can calculate the most important metallurgical variables such as the fusion zone geometry, temperature and velocity fields, cooling rates and solidification parameters for multi-layer, multi-hatch builds for various AM variables.

In part I of this paper, a 3D transient heat transfer and fluid flow model of PBF-AM was developed and tested. The model solves the equations of conservation of mass, momentum and energy to calculate temperature and velocity fields, build shape and size and cooling rates from the process parameters and alloy properties. The model considers the convective flow of liquid metal inside the molten pool that is often the main mechanism of heat transfer within the liquid pool. The model also takes into account temperature dependent powder bed properties calculated based on powder particle size and packing efficiency. A travelling grid system is used to enhance the computational efficiency for multi-layer, multi-hatch calculations. Here the model is applied to calculate temperature and velocity fields, fusion zone shape and size, cooling rates, solidification parameters, arm spacing of columnar dendrites, micro-hardness, susceptibility to lack of fusion defects and distortion. The calculations are done for multi-layer, multi-hatch builds of four commonly used alloys, stainless steel 316 (SS 316), Ti-6Al-4V, Inconel 718 (IN 718) and AlSi10Mg.

2. Results and discussions

Table 1 lists the properties of the powders [23] used in the calculations. The computational domain (in Fig. 1) consists of powder bed, substrate and 5 layers, 5 hatches, build. The X-, Y- and Z- directions represent the scanning, hatching and building directions, respectively. For simplicity, a unidirectional scanning strategy is considered where the laser beam travels along the positive X-direction for all layers and hatches. Process variables and dimensions of the computational domain used in calculations are provided in Table 2.

2.1. Temperature and velocity fields

Fig. 2 shows the computed temperature and velocity fields during the building of the first layer first hatch with four different alloy powders. The red colored region bounded by the liquidus temperature isotherm of an alloy represents the fusion zone of the molten pool. The green colored region within the liquidus and the solidus temperature isotherms represents the mushy zone. Since the laser beam travels in the direction of positive X-axis, the molten pool is elongated in the opposite direction (negative X-axis). The molten pool exhibits a teardrop shape that is attributed to rapid scanning speed commonly used in the PBF process. The computed velocity vectors within the molten pool are shown by black arrows. The magnitude of these velocity vectors can be found out by comparing their length with the reference vector provided. The velocity vectors are radially outward as molten metal flows in the direction of positive temperature gradient [22–27]. For a

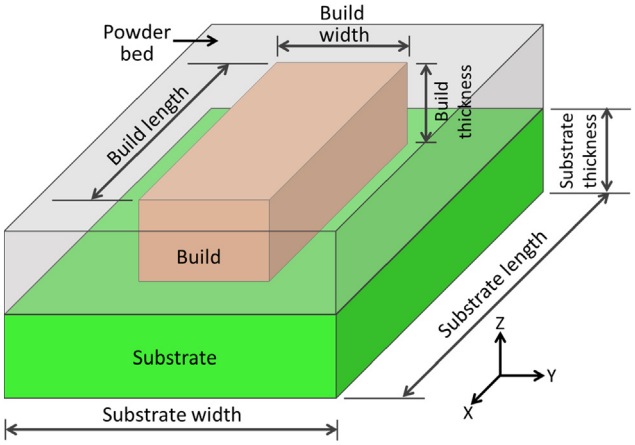

Fig. 1. Schematic of the solution domain consisting of substrate, powder bed and build. X, Y and Z directions represent the scanning, hatching and building directions, respectively.

Table 2
Process parameters used for calculations.

Parameter set	1	2
Laser power, W	60	110
Scanning speed, mm/s	250–1000	100
Spot radius, mm	0.05	0.30
Layer thickness, mm	0.025–0.035	0.30
Hatch spacing, mm	0.035–0.105	0.30
Build length, mm	20	5.28
Substrate dimensions, mm × mm × mm	22 × 5 × 2	7.17 × 4 × 1
Packing efficiency	0.5	0.4

Table 1
Thermo-physical properties of SS 316, Ti-6Al-4V, IN 718 and AlSi10Mg [23]. Here 'T' represents temperature in K ranging from ambient to the solidus temperature.

Properties	SS 316	Ti-6Al-4V	IN 718	AlSi10Mg
Liquidus temperature (K)	1733	1928	1609	867
Solidus temperature (K)	1693	1878	1533	831
Thermal conductivity (W/m K)	$11.82 + 1.06 \times 10^{-2}\,T$	$1.57 + 1.6 \times 10^{-2}\,T - 1 \times 10^{-6}\,T^2$	$0.56 + 2.9 \times 10^{-2}\,T - 7 \times 10^{-6}\,T^2$	$113 + 1.06 \times 10^{-5}\,T$
Specific heat (J/kg K)	$330.9 + 0.563\,T - 4.015 \times 10^{-4}\,T^2 + 9.465 \times 10^{-8}\,T^3$	$492.4 + 0.025\,T - 4.18 \times 10^{-6}\,T^2$	$360.4 + 0.026\,T - 4 \times 10^{-6}\,T^2$	$536.2 + 0.035\,T$
Density (kg/m^3)	7800	4000	8100	2670
Latent heat of fusion (J/kg)	272×10^3	284×10^3	209×10^3	423×10^3
Viscosity (kg/m s)	7×10^{-3}	4×10^{-3}	5×10^{-3}	1.3×10^{-3}
$d\gamma/dT$ (N/m K)	-0.40×10^{-3}	-0.26×10^{-3}	-0.37×10^{-3}	-0.35×10^{-3}
Absorption coefficient in liquid (η_l)	0.3	0.3	0.3	0.3
Absorption coefficient in powder (η_P)	0.7	0.7	0.7	0.7
Volumetric expansion coefficient (/K)	5.85×10^{-5}	2.5×10^{-5}	4.8×10^{-5}	2.4×10^{-5}
Young's modulus (GPa)	206	110	207	68

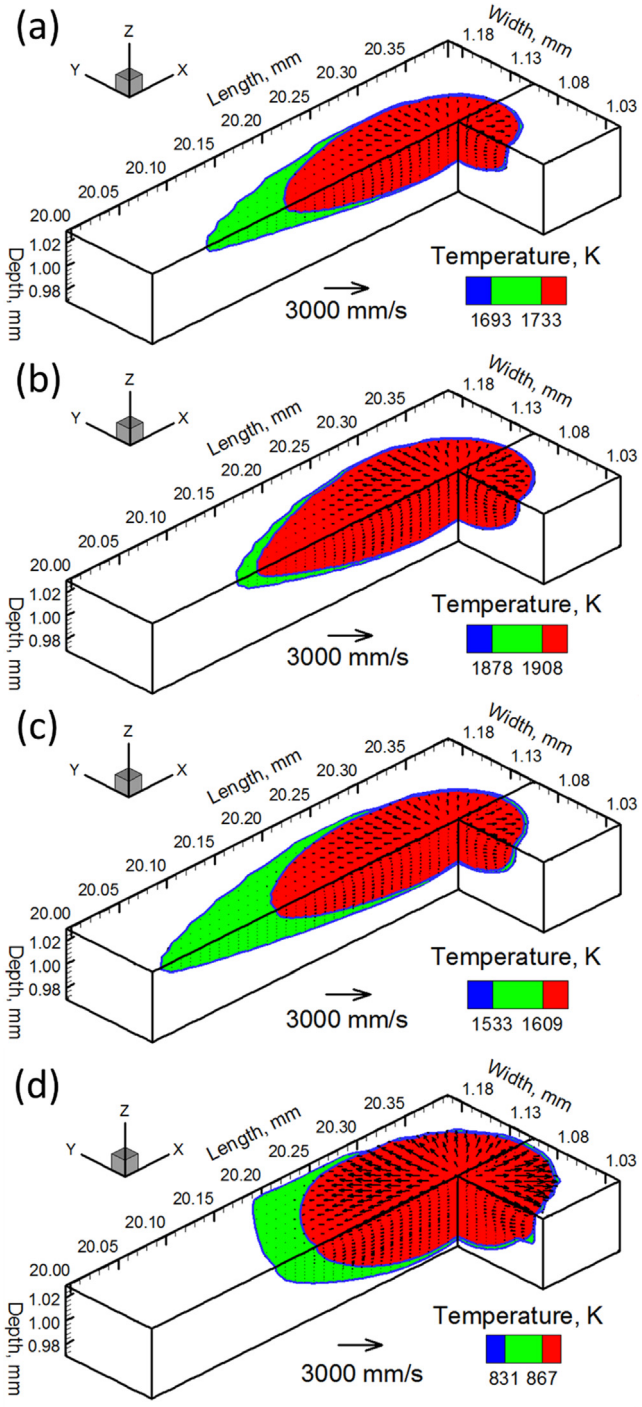

Fig. 2. Three-dimensional temperature and velocity distributions in the 1st layer 1st hatch of 20 mm long build of (a) SS 316 (b) Ti-6Al-4V (c) IN 718 and (d) AlSi10Mg using 1000 mm/s scanning speed. Other process conditions are same as process parameter set 1 of Table 2. Scanning direction of the laser beam is along the positive x-axis.

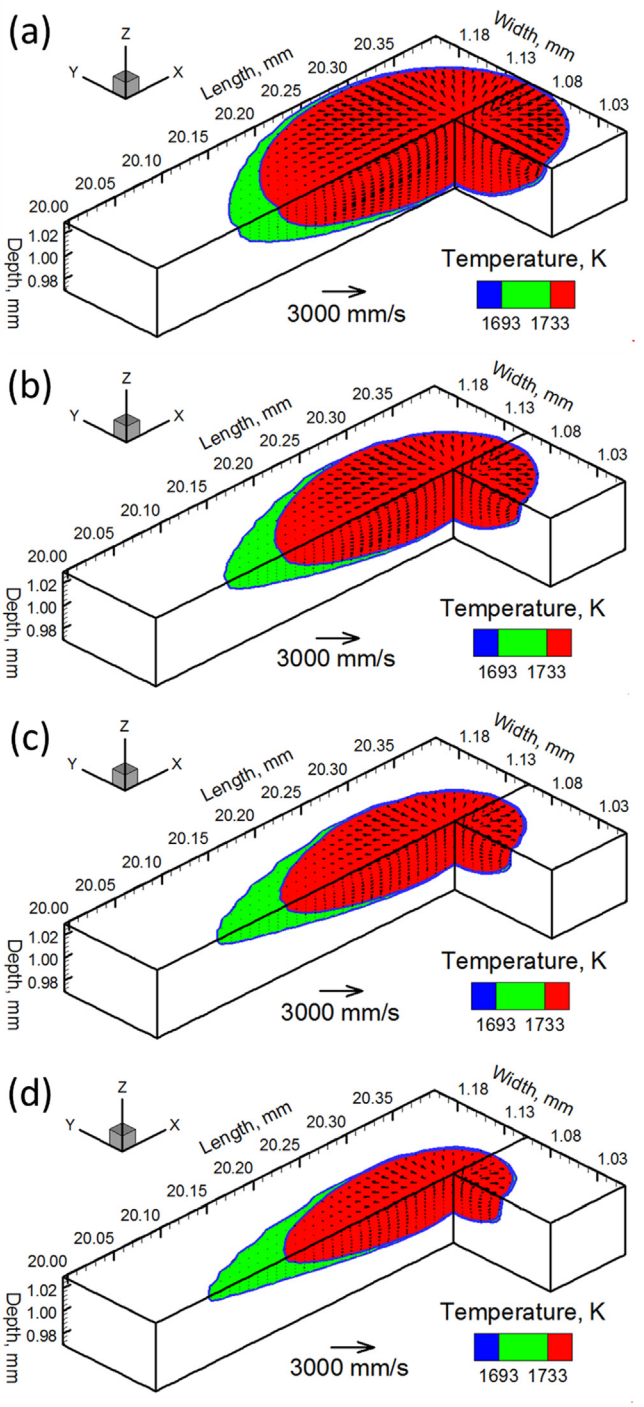

Fig. 3. Three-dimensional temperature and velocity distributions in the 1st layer 1st hatch of 20 mm long build of SS 316 using laser scanning speed of (a) 250 (b) 500 (c) 750 and (d) 1000 mm/s. Other process conditions are same as parameter set 1 of Table 2. Scanning direction of the laser beam is along the positive x-axis.

given processing condition, AlSi10Mg build exhibits the largest molten pool due to its lowest density and liquidus temperature. The build with IN 718 alloy powder results in largest mushy zone due to the maximum temperature range between the liquidus and solidus temperatures. Fig. 3(a–d) shows the computed temperature and velocity fields for first layer, first hatch of SS 316 build at four different laser scanning speeds. As shown in figure, the size of the molten pool decreases with increase in scanning speed that is attributed to lower heat input at faster scanning speeds.

Fig. 4(a) shows the variation in temperature with time (thermal cycle) for a location at mid-length and on the top surface of first layer, first hatch of the builds of four alloy powders using the same process parameters. The peak temperature is attained at a time of 2 ms when the laser beam reaches on the top of the location. The small knee, noted in the thermal cycle between the liquidus and solidus temperatures of different alloys, is referred as the thermal arrest during solidification. The highest peak temperature for the Ti-6Al-4V build is attributed to its lowest density. However, the AlSi10Mg build exhibits the lowest peak

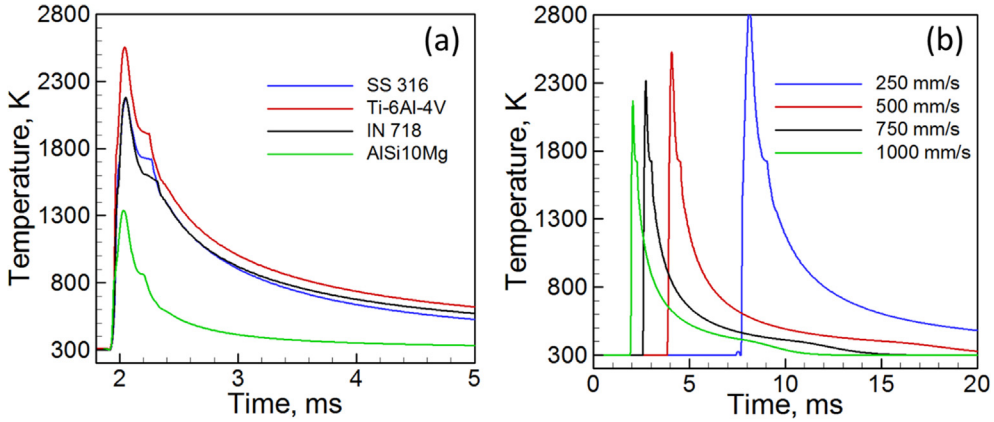

Fig. 4. Temperature variation with time for a location on the top surface and at the mid length of first layer, first hatch of the build (a) of four different alloys using 1000 mm/s scanning speed and (b) of SS 316 using four different scanning speeds. Other process conditions are same as parameter set 1 of Table 2.

temperature because of its highest thermal diffusivity. The influence of laser scanning speed on thermal cycle while fabricating first layer, first hatch of a SS 316 build is explained in Fig. 4(b). Different scanning speeds allow the laser beam to reach to the pre-defined location at different time instants. Therefore, the peak temperature is attained at different time for different scanning speeds. Faster scanning reduces the net amount of heat input resulting in a lower peak temperature.

During the fabrication of a multi-layer, multi-hatch build, a particular location experiences repeated heating and cooling depending on the sequence and pattern of hatching process. Fig. 5(a) shows the variation in temperature with time for a location at mid-length and on the top surface of the first hatch during the fabrication of a single layer, 10 hatches SS 316 build. As the laser beam moves away from the first hatch to build the neighboring hatches, the peak temperature reduces at that monitoring location. Fig. 5(b) shows the variation in temperature for the same location during the fabrication of a three layers, three hatches SS 316 build. As the three hatches of the first layer are build, peak temperature at the considered location decreases as observed in Fig. 5(a). At the end of building the first layer, the laser beam returns to the top of the first hatch to build the second layer. That results in rise in the peak temperature of the location. A similar pattern continues during the building of subsequent hatches and layers.

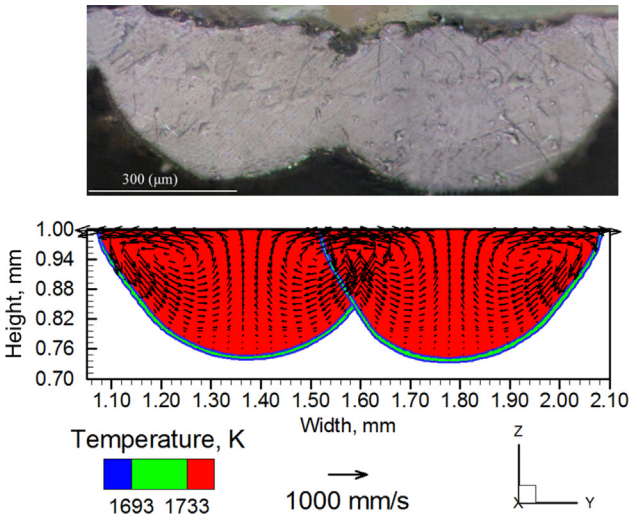

Fig. 6. Comparison between the calculated and experimentally [28] observed transverse section of the SS 316 single layer multi-hatch build fabricated using the process parameter set 2 of Table 2.

2.2. Fusion zone geometry

The depth and width of a particular hatch can be found from the largest transverse cross-section (in YZ-plane) of the three-dimensional pool (Figs. 2 and 3). Fig. 6 shows a fair agreement between the computed and the corresponding measured [28] build shapes and sizes for two neighboring hatches of a single layer SS 316 build.

Fig. 7(a) summarizes the effects of scanning speed on pool volume during fabrication of the first layer, first hatch of the builds with four alloy powders. Decrease in pool volume with faster scanning speed is attributed to reduced heat input at higher scanning speeds. Lowest density and liquidus temperature of AlSi10Mg result in largest pool size as shown in Fig. 7(a). Thermo-physical properties of SS 316 and IN 718 are nearly similar. However, IN 718 exhibits slightly larger pool than SS 316 because of smaller latent heat of fusion of IN 718. Smaller density of Ti-6Al-4V alloy powder results in larger molten pool size in

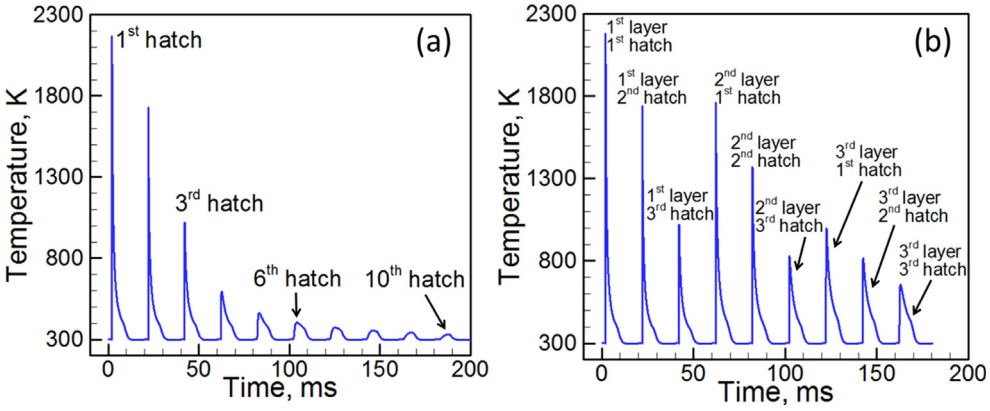

Fig. 5. Temperature variation with time for a location on the top surface and at the mid length of the 1st layer 1st hatch during the fabrication of (a) a single layer, 10 hatches SS 316 build using 1000 mm/s speed (b) a 3 layers, 3 hatches SS 316 build using 1000 mm/s speed. Other process conditions are same as parameter set 1 of Table 2.

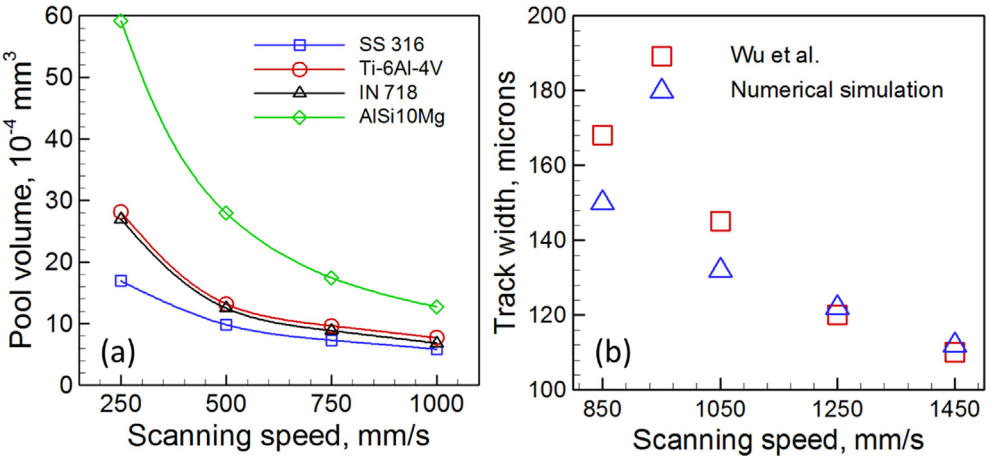

Fig. 7. (a) Effect of scanning speed on pool volume calculated at the mid-length of 1st layer 1st hatch for 4 different alloys. Process conditions are same as parameter set 1 of Table 2. (b) Comparison between the calculated and experimentally [29] observed track width of a single layer single hatch Ti-6Al-4V build at different scanning speeds.

comparison to that for SS 316. Fairly high laser scanning speeds are common in PBF processes to reduce the overall time to build a multi-layer, multi-hatch, part. At very high scanning speeds, the heat transfer is primarily influenced by the scanning speed in the direction of travel of the laser beam (along X-direction). As a result, the differences in pool sizes for different alloys are less pronounced at higher scanning speeds as observed in Fig. 7(a). Fig. 7(b) shows that the calculated track width and its variation with scanning speed for a single layer single hatch Ti-6Al-4V build agree well with independent experimental observations [29].

Heat transfer from the molten pool governs the spatially non-uniform and transient temperature distribution and affects the build geometry, cooling rates, solidification parameters, microstructure, properties and defect formation [30]. For a multi-layer, multi-hatch build, the primary direction of heat transfer from the molten pool changes continuously as different hatches and layers are built. Fig. 8 schematically represents the heat transfer pattern from the molten pool for multi-layer multi-hatch build. Fig. 8(a) shows that for the first layer first hatch, maximum amount of heat is transferred from the molten pool through the substrate, since the thermal conductivity of substrate is significantly higher than that for powder bed. Due to the higher thermal conductivity of the solid build than the powder bed, maximum heat transfer occurs from the molten pool to the substrate through the already deposited layers during the building of higher layers as shown in Fig. 8(b). Since the distance between the molten pool and the substrate increases with layer number, rate of heat loss decreases for the upper layers. However, the rate of heat transfer would tend to attain a plateau beyond a certain height depending on the solidified build geometry, processing conditions and the thermo-physical properties of the alloy. In addition, heat accumulation in the build also increases as more layers are added and heat is continuously supplied to the growing component. As a result, the temperature of the build increases. During the fabrication of the first hatch of a particular layer, the molten pool has powder bed on both sides. However, for the other hatches, one side of the molten pool is already built and the other side is still powder bed (as shown in Fig. 8(c)). Therefore, the heat transfer for the subsequent hatches increases from the first hatch because of the high thermal conductivity of the already built hatch on one side.

The differences in heat transfer patterns in different layers and hatches result in changing volume of the liquid pool as shown in Fig. 9.

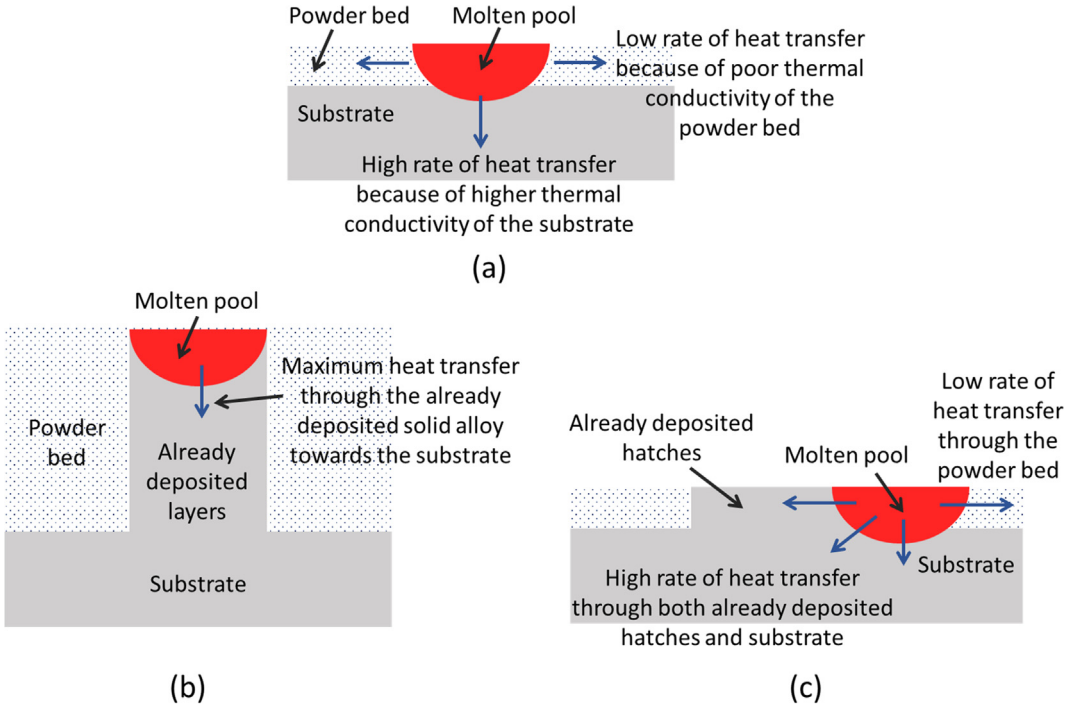

Fig. 8. Schematic of heat transfer from the molten pool for (a) 1st layer 1st hatch (b) higher layers and (c) higher hatches.

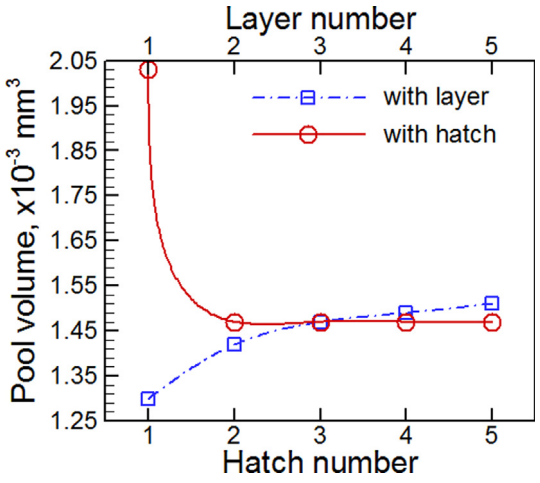

Fig. 9. Variation of molten pool volume with layer number at 3rd hatch and with hatch number for 3rd layer for a 5 layers 5 hatches SS 316 build using 1000 mm/s scanning speed. Other process conditions are same as parameter set 1 of Table 2. Pool volumes are calculated at the mid-legth of a particular track.

The pool volume increases in the upper layers because of reduced rate of heat transfer further away from the substrate. During the building of the second hatch, one side of the pool faces the solidified build which has a higher thermal conductivity. As a result, the volume of the liquid pool in the second hatch is smaller than that of the first hatch. In the subsequent hatches, the liquid pool volume does not significantly change because the heat transfer pattern remains the same in the subsequent hatches. This result is consistent with the experimental observation [31].

Fig. 10(a) and (b) shows the transverse view (YZ plane) of the molten pool for the first and second hatches along the first layer of a SS 316 build. The solidus temperature isotherm (1693 K) represents the molten pool boundary. The distances of the right and left sides of the molten pool boundary from the laser beam axis are denoted as 'R' and 'L' respectively. Both sides of the molten pool are powder bed during

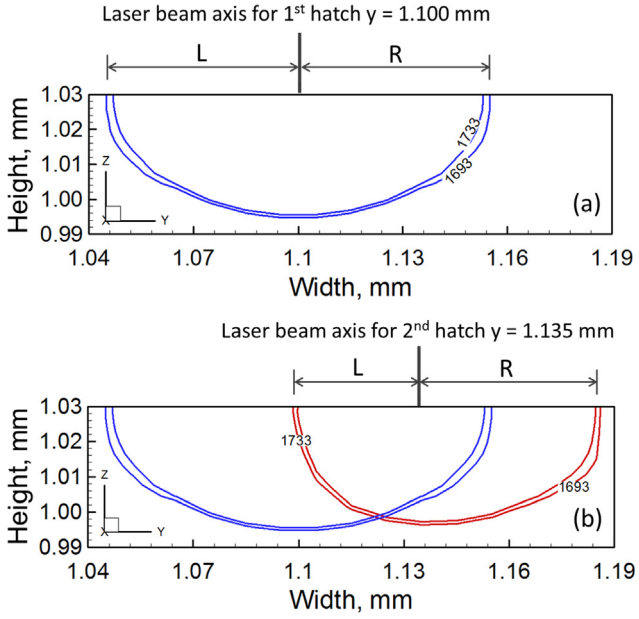

Fig. 10. Transverse sectional view of the molten pool at the mid-length for (a) 1st hatch (blue) and (b) both 1st (blue) and 2nd hatch (red) of SS 316 build using 1000 mm/s scanning speed. Other process conditions are same as parameter set 1 of Table 2. (For interpretation of the references to colour in this figure legend, the reader is referred to the web version of this article.)

building the first hatch. This symmetry results in similar rate of heat transfer to both the sides and a symmetrical cross section of the molten pool as observed by R = L. During building of the second hatch with the solid build on its left and the powder bed on its right, heat transfer is significantly asymmetric because of the higher thermal conductivity of the solidified build. This difference in heat transfer is reflected in a pronounced asymmetry of the cross section as indicated by R > L. The extent of asymmetry of the molten pool is represented by an asymmetry ratio (AR) as:

$$AR = R/L \tag{1}$$

where the value of 'AR' is one for the first hatch and less than one for the subsequent hatches. Since, asymmetry of the molten pool controls the molten pool shape, it affects the fusional bonding between two successive hatches and layers.

Fig. 11(a) shows that the extent of asymmetry (AR) of the molten pool does not change for the second and subsequent hatches as expected. The asymmetry depends on the heat transfer conditions on both sides of the molten pool. Furthermore, it does not change significantly as more layers are built. The influence of scanning speed on pool asymmetry is shown in Fig. 11(b). At higher scanning speeds, the liquid pool is narrower because of the low heat input per unit length. As a result, the asymmetry is magnified as shown in the figure. Alloys with high thermal diffusivity exhibits more uniform heat dissipation at all sides of the molten pool that reduces the pool asymmetry. Therefore, AlSi10Mg and SS 316 has the lowest and highest asymmetry, respectively, among the four alloys considered.

With increasing packing efficiency of the powder bed, the thermophysical properties of the powder bed approach to that of the solid alloy that also results in lower asymmetry of the liquid pool as shown in Fig. 11(c). In contrast, the heat transfer pattern from the molten pool does not change significantly with small increase in hatch spacing. Therefore, the asymmetry of the molten pool remains almost unchanged when the hatch spacing is increased from 25 to 65 μm as observed in Fig. 11(d). However, neighboring molten pools start to separate from each other beyond a hatch spacing of 65 μm. When the hatch spacing exceeds 65 μm, the extent of overlapping is continuously reduced and at a hatch spacing of 105 μm, the two neighboring molten pools completely separate from each other and behave as independent hatches with powder on both sides. As a result, separate fusion tracks with symmetrical liquid pool forms.

2.3. Solidification parameters, dendrite arm spacing and hardness

The temperature gradient between liquidus and solidus temperature, G and the solidification growth rate, R, provide insightful information about the evolution of the solidification structure [32]. The term, GR provides the cooling rate during solidification and the ratio G/R indicates the morphology of the solidification front. Columnar dendrites are often observed during the PBF of different alloys. Secondary dendritic arm spacing, SDAS (λ) of the columnar dendrites can be calculated from the cooling rates (GR) [33].

$$\lambda = A(GR)^{-n} \tag{2}$$

where SDAS (λ) is in μm, cooling rate (GR) is in K/s and A and n are the material specific constants, whose values are 50 and 0.4, respectively, for SS 316 [34] and 43 and 0.32, respectively, for AlSi10Mg [35]. For very fine columnar dendritic structure, the yield strength (σ_Y) can be correlated with the secondary dendritic arm spacing (λ) using Hall-Petch like equation as [33],

$$\sigma_Y = \sigma_o + K(\lambda)^{-0.5} \tag{3}$$

where yield strength (σ_Y) is in MPa, σ_o and K are the material specific constants, whose values are 240 MPa and 279 MPa (μm)$^{0.5}$, respectively, for SS 316 [34] and 36 MPa and 167 MPa (μm)$^{0.5}$, respectively, for AlSi10Mg [36]. The average micro-hardness (H) is related to the

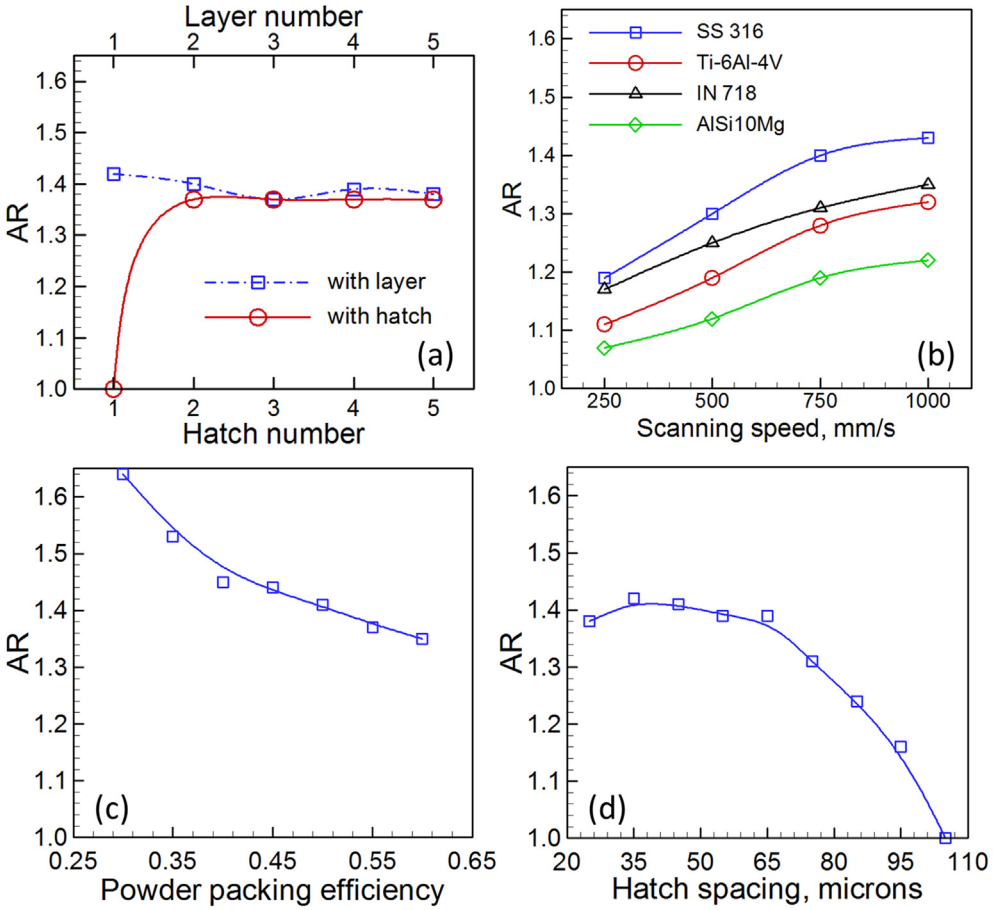

Fig. 11. Variations of the asymmetry ratio (AR) with (a) layer number at 3rd hatch and with hatch number at 3rd layer (b) scanning speed for 4 different alloys (c) powder packing efficiency and (d) hatch spacing at 1st layer 3rd hatch. Calculations for figures (a), (c) and (d) are done using 1000 mm/s scanning speed. All results are for a 5 layers 5 hatches SS 316 build. Other process conditions are same as parameter set 1 of Table 2.

yield strength (σ_Y) as [33],

$$H = 3\sigma_Y (0.1)^{-m} \tag{4}$$

where m is a material specific constant whose value is 0.25 and 0.21 for SS 316 and AlSi10Mg, respectively [33].

Fig. 12(a) and (b) show the cooling rate during solidification, GR, and the morphological parameter, G/R, respectively, for different alloys. Among the four alloys, the AlSi10Mg build exhibits the largest molten pool. Therefore, the cooling rate and G/R of AlSi10Mg build are the lowest among the four alloys. The SS 316 and IN 718 builds show around same cooling rate and G/R because of their almost identical thermo-physical properties. For the same processing conditions, the Ti-6Al-4V build experiences the highest cooling rate and G/R because of its high thermal diffusivity.

Rapid scanning decreases the heat input per unit time. Therefore, faster scanning speed results in smaller molten pool that cools and solidifies rapidly. Therefore, cooling rate during solidification increases with laser scanning speed as shown in Fig. 13(a). Fig. 13(b) shows that the calculated cooling rates during solidification of a single layer single hatch SS 316 build for various linear heat input agree reasonably well with the corresponding experimental data [4]. In this figure the linear heat input denotes amount of energy supplied per unit length of the build and is obtained from the ratio of laser power to scanning speed. Since, higher heat input results in larger molten pool, cooling rate decreases with heat input as shown in Fig. 13(b). Fig. 13(c) shows that faster scanning speed results in lower G/R which is an indicator of the morphology of the solidified structure. Faster scanning speed results in higher growth rate that reduces G/R during solidification, as shown in

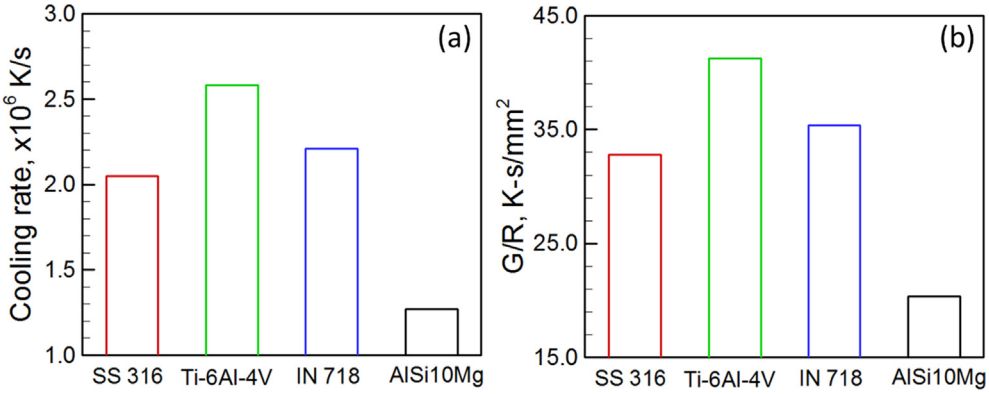

Fig. 12. (a) Cooling rate and (b) G/R during solidification calculated at mid-length and on the top surface of 3rd layer 3rd hatch of 5 layers 5 hatches builds of 4 alloys using 250 mm/s scanning speed. Other process conditions are same as parameter set 1 of Table 2.

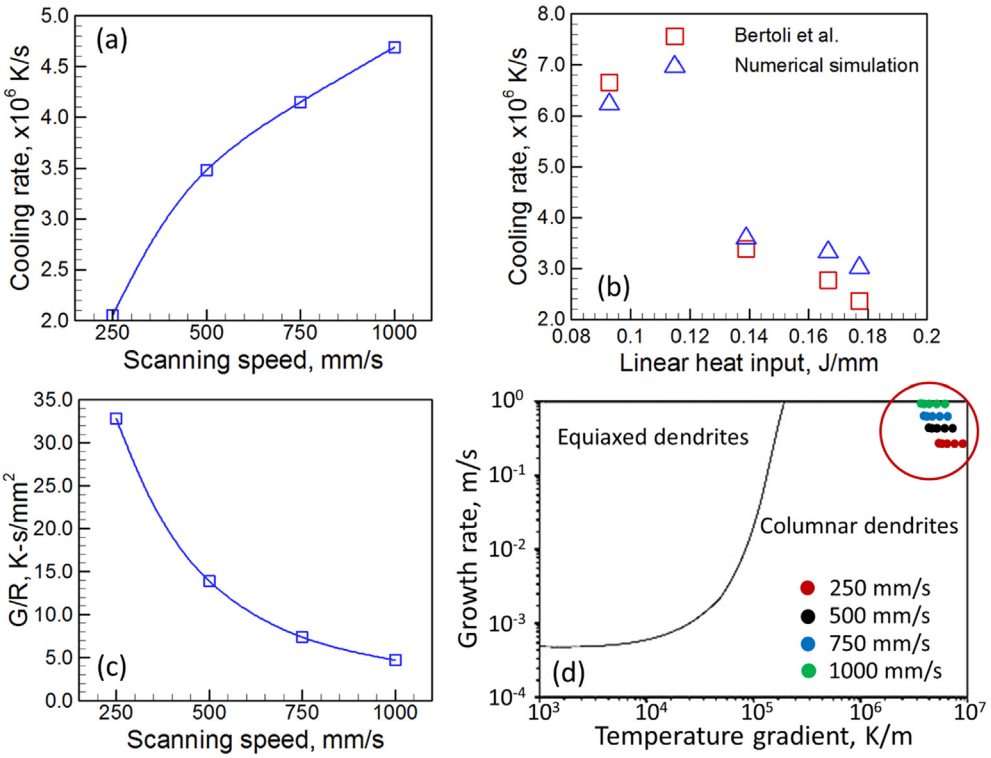

Fig. 13. (a) Variation of cooling rate with scanning speed at 3rd layer 3rd hatch using 250 mm/s scanning speed. (b) Comparison between the calculated and experimentally [4] observed cooling rates of a single-track build at different heat inputs. (c) Variation of G/R with scanning speed at 3rd layer 3rd hatch using 250 mm/s scanning speed. (d) Calculated values of temperature gradient (G) and growth rate (R) at four different scanning speeds on the solidification map [37]. Calculations for figures (a), (c) and (d) are done for a 5 layers 5 hatches build. Other process conditions are same as parameter set 1 of Table 2. All results are for SS 316 and calculated at mid-length and on the top surface of the track during solidification.

this figure. The ratio G/R between the liquidus and solidus temperature of alloy indicates the solidification morphology. Therefore, the values of temperature gradient (G) and growth rate (R) for five layers of a SS 316 build using four different scanning speeds are plotted in a solidification map (growth rate vs. temperature gradient plot) [37] in Fig. 13(d). All data at various scanning speeds are inside the red circle. The data indicate that columnar dendrites are observed in the PBF of SS 316. Under similar processing conditions, columnar dendrites are also experimentally observed during PBF of SS 316 in other investigations [38]. Columnar dendritic morphology is also very common in PBF components of AlSi10Mg [35].

Fig. 14(a) and (b) shows the effects of scanning speed on the calculated SDAS and hardness (in Vickers scale), respectively. Higher scanning speed results in smaller pool and faster cooling rates. Therefore, SDAS of columnar dendrites decreases with increasing scanning speed as shown in Fig. 14(a). Smaller SDAS increases both the mechanical strength and hardness of the solidified structure. Therefore, hardness of the component is enhanced by fabricating it with higher scanning speed as shown in Fig. 14(b). The calculated values of hardness for both the alloys agree well with the reported values in the literature [39,40] for similar processing conditions.

Fig. 15(a) and (b) shows the cooling rate and G/R for various layers and hatches. Both cooling rate and G/R are computed on the top surface and at the mid-length and mid-width of a track. The cooling rate and G/R increase from first to second hatch but subsequently become nearly insensitive after building the second hatch. This is attributed to slight increase in heat transfer rate from the first to the second hatch along any layer as solid metal is deposited on one side. In contrast, both the cooling rate and G/R along a specific hatch decrease in the upper layers due to reduced heat loss to the substrate and increased heat accumulation in the upper layers.

Thicker layers and larger hatch spacing may result in rapid production but require higher heat input causing dimensional inconsistency and defect formation. An appropriate selection of layer

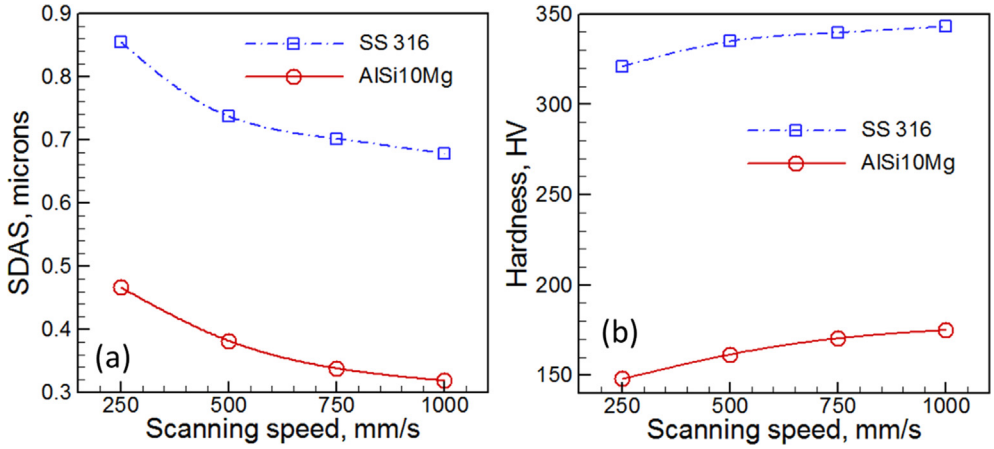

Fig. 14. Variation of (a) secondary dendrite arm spacing (SDAS) and (b) Vickers hardness with scanning speed calculated at mid-length and on the top surface of 1st layer 1st hatch of SS 316 and AlSi10Mg builds. Other process conditions are same as parameter set 1 of Table 2.

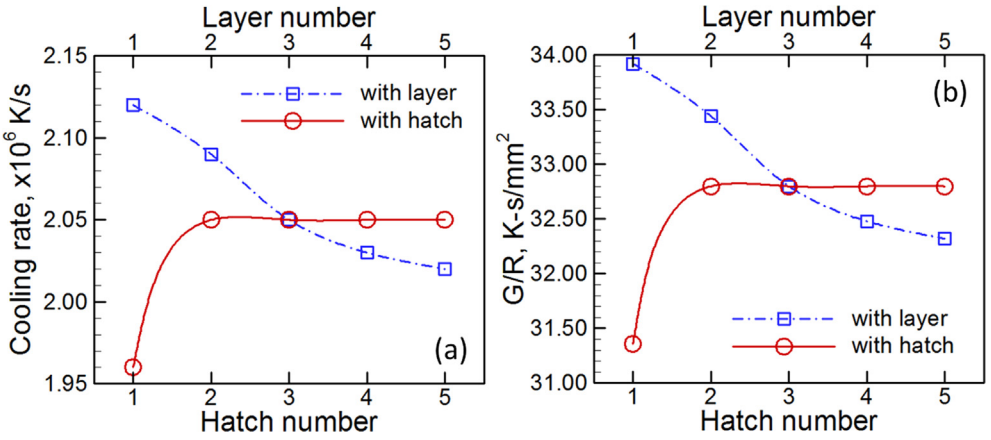

Fig. 15. Variation of (a) cooling rate and (b) G/R during solidification with layer number at 3rd hatch and with hatch number for 3rd layer for a 5 layers 5 hatches SS 316 build using 250 mm/s scanning speed. Calculations are done at the mid-length and on the top surface of track. Other process conditions are same as parameter set 1 of Table 2.

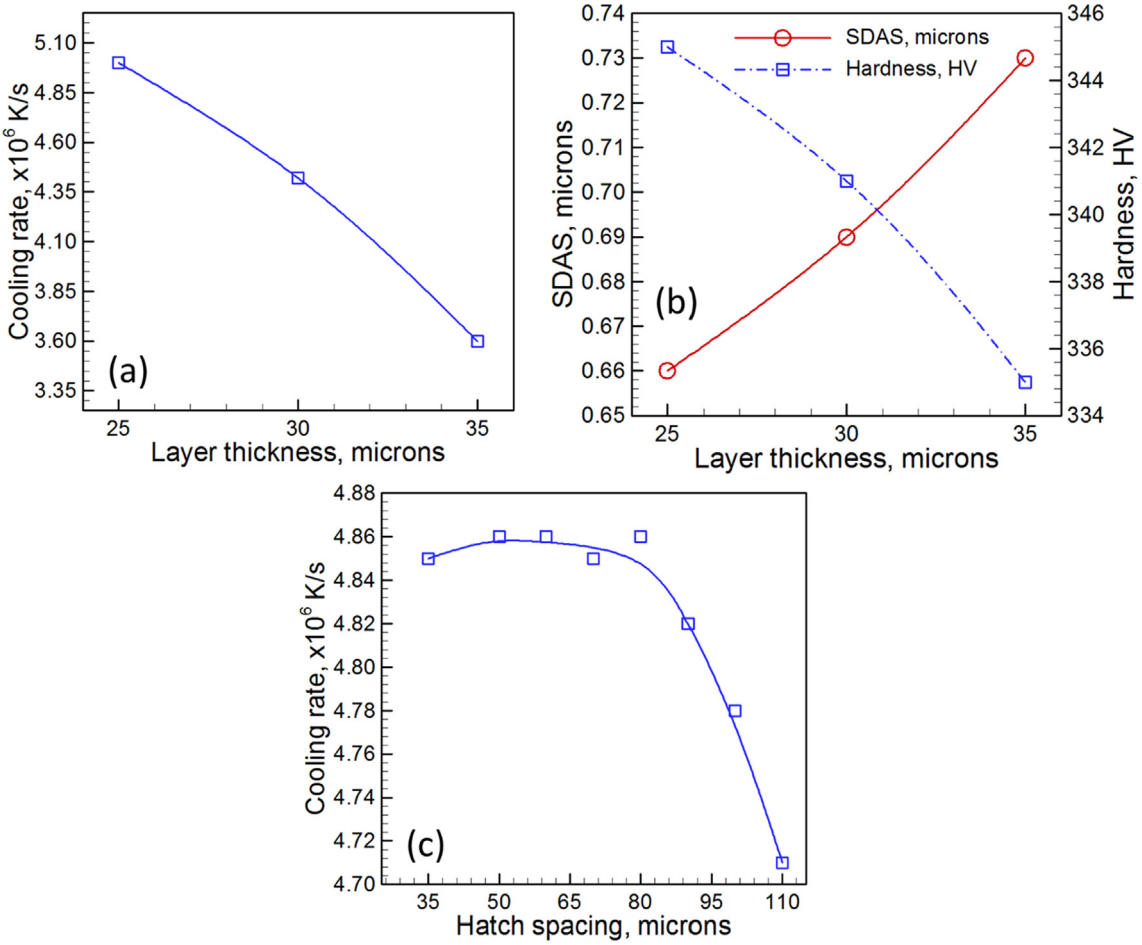

Fig. 16. Effects of layer thickness on (a) cooling rate (b) secondary dendritic arm spacing (SDAS) and Vickers hardness calculated at 3rd layer 1st hatch. (c) Effects of hatch spacing on cooling rate at 1st layer 3rd hatch. Cooling rates are calculated during solidification. All calculations are done at the mid-length and on the top surface of the track for a 5 layers 5 hatches SS 316 build using 1000 mm/s scanning speed. Other process conditions are same as parameter set 1 of Table 2.

thickness and hatch spacing is important for rapidly manufacturing defect free components with desired structure and properties. Fig. 16(a) shows the computed cooling rates during solidification. A build made of thicker layers absorbs more heat. In addition, thicker layers reduces the rate of heat transfer from the molten pool to the surroundings. Therefore, cooling rate during solidification decreases with increasing layer thickness, as shown in Fig. 16(a). Lower cooling rate with thicker layers results in increased SDAS and reduced micro-hardness as shown in Fig. 16(b). Change in hatch spacing shows little effect on the computed cooling rate as long as the molten pools of neighboring hatches overlap adequately. For example, the solidification cooling rate remains nearly unchanged for increase in hatch spacing from 35 to 70 μm as shown in Fig. 15(c). However, for hatch spacing more than 70 μm, the molten pools of neighboring hatches start separating that reduces the heat transfer from the molten pool. Therefore, a sharp decrease in cooling rate during solidification is observed at hatch spacings greater than 70 μm.

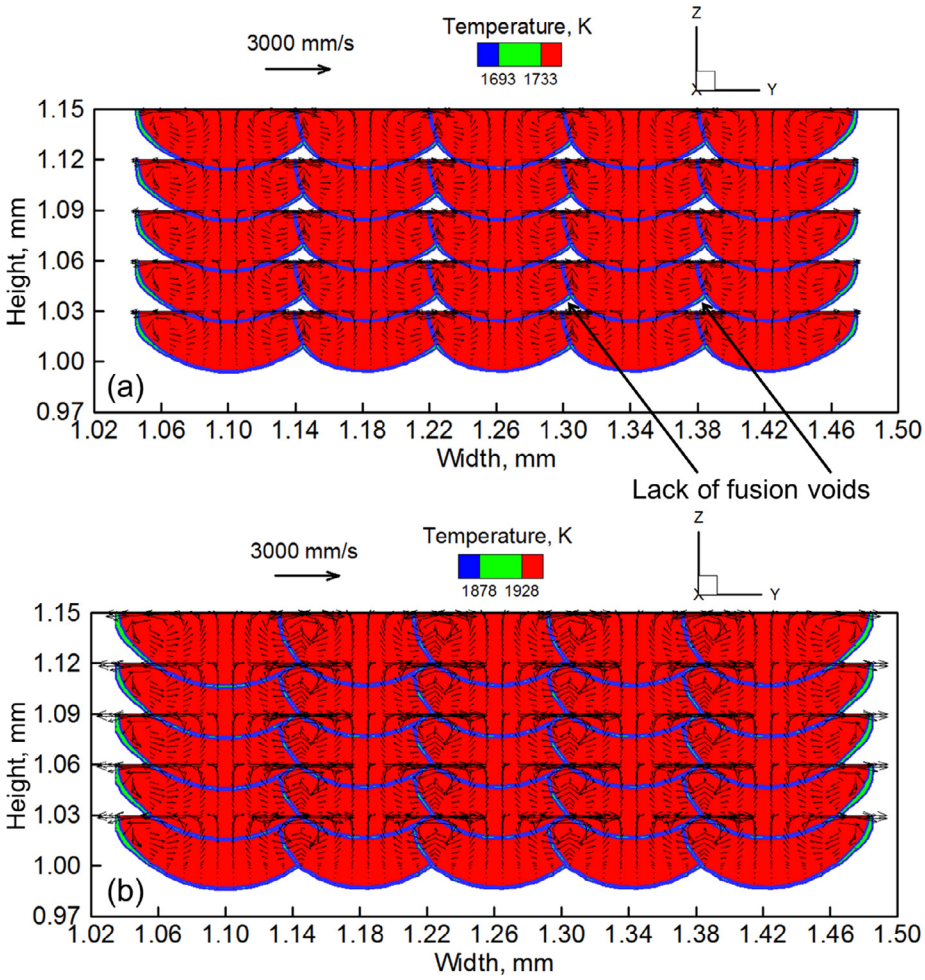

Fig. 17. Transverse sectional view of the molten pools for 5 layers 5 hatches build of (a) SS 316 (b) Ti-6Al-4V build using 1000 mm/s scanning speed and 80 μm hatch spacing. Other process conditions are same as parameter set 1 of Table 2.

2.4. Lack of fusion defects

Lack of fusion defects originate from improper fusional bonding between hatches and layers [1]. Therefore, these defects depend on width and depth of the molten pool, layer thickness and hatch spacing. Fig. 17(a) and (b) shows the computed shapes and sizes of the molten pool transverse sections (YZ plane) for different hatches and layers of five hatch, five layer, builds of SS 316 and Ti-6Al-4V, respectively. For the SS 316 build, unmelted regions between the molten pools indicating improper fusional bonding among layers and hatches represent the lack of fusion voids. For the same processing conditions, molten pools in Ti-6Al-4V build are much larger in size and prevent lack of fusion defects as observed in Fig. 17(b).

Fig. 18(a) and (b) shows the effect of hatch spacing on the lack of fusion voids. The percentage of lack of fusion voids is calculated as a ratio of area in the unmelted region to the total area of cross section of the build expressed in percentage. Higher hatch spacing results in improper fusional bonding between two successive hatches and increases the amount of lack

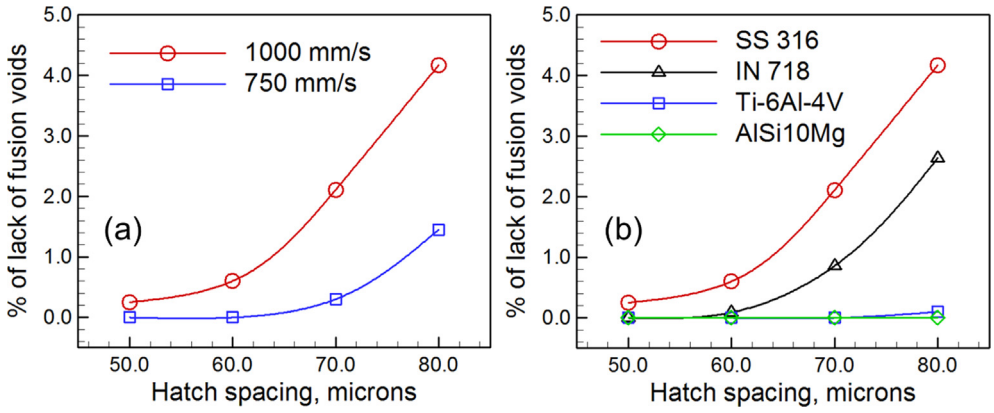

Fig. 18. Variation of amount of lack of fusion voids with hatch spacing for 5 layers 5 hatches build of (a) SS 316 using 750 mm/s and 1000 mm/s scanning speeds and (b) 4 alloys using 1000 mm/s scanning speed. Other process conditions are same as parameter set 1 of Table 2.

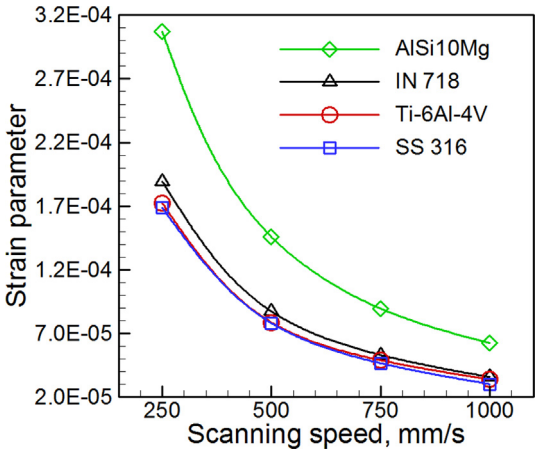

Fig. 19. Variation of the strain parameter with scanning speed during the fabrication of 1st layer 1st hatch of builds of four alloys. Other process conditions are same as parameter set 1 of Table 2.

of fusion voids. At a given hatch spacing, the lack of fusion voids can be minimized by increasing the overlapping of the fused regions. This can be accomplished by increasing the size of the molten pool at lower scanning speeds as shown in Fig. 18(a). Therefore, for a particular alloy component the lack of fusion defects can be minimized by reducing the scanning speed and/or hatch spacing. Among the four alloys, SS 316 exhibits the smallest molten pool. Therefore, under same processing conditions, SS 316 requires the smallest hatch spacing to prevent lack of fusion defect as shown in Fig. 18(b).

2.5. Distortion

Spatially non-uniform and transient temperature field in PBF can result in thermal distortion resulting in dimensional inaccuracy and part rejection [1]. The extent of thermal distortion of the final build would be affected primarily by the AM process variables and a few key properties of the alloy powder. Recently, it has been shown that the distortion of the AM parts can be quantitatively represented by a strain parameter (ε^*) as [2,3,41]:

$$\varepsilon^* = \frac{\beta \Delta T}{EI} \frac{t}{F\sqrt{\rho}} H^{3/2} \tag{5}$$

where β is the co-efficient of volumetric expansion and ΔT is the difference between the peak temperature and ambient temperature, t is the total building time, H is the heat input per unit length of the build, EI is the flexural rigidity of the substrate, F is the Fourier number [33] and ρ is the density of alloy.

Fig. 19 shows the effect of the laser scanning speed on the calculated strain parameter. Faster scanning speed results in smaller molten pool, smaller volume shrinkage during solidification and reduced strain. Among the four alloys, the susceptibility to thermal distortion is highest for AlSi10Mg due to the largest pool volume under the same processing conditions. Although Ti-6Al-4V exhibits bigger molten pool than SS 316, its volumetric thermal expansion co-efficient is about half of that for SS 316. Therefore, calculated strain values of Ti-6Al-4V and SS 316 build are almost the same. SS 316 and IN 718 builds exhibit nearly the same strain due to their similar thermo-physical and mechanical properties. However, strain values for these alloys in PBF are much lower than that for direct energy deposition [2,3] because of the smaller molten pool of the PBF process.

3. Summary and conclusions

A 3D transient heat transfer and fluid flow model of powder bed fusion AM is developed and tested in the first part of this paper. The validated mathematical framework is utilized here to calculate the parameters that affect the metallurgical quality of the component. These parameters include temperature and velocity fields, fusion zone shape and size, cooling rates, solidification parameters, dendrite arm spacing, micro-hardness and susceptibility to lack of fusion defect and distortion. Calculations are done for multi-layer, multi-hatch builds of four alloys widely used in AM, SS 316, Ti-6Al-4V, IN 718 and AlSi10Mg. Below are the specific findings.

(1) Rapid scanning reduces distortion of the component and promotes dimensional accuracy. Among the four alloys, AlSi10Mg is the most susceptible to thermal distortion because of its largest molten pool that shrinks considerably during solidification.
(2) Among the four alloys, SS 316 requires the smallest hatch spacing to prevent lack of fusion defect. However, the biggest molten pool of AlSi10Mg ensures proper fusional bonding among layers and hatches that minimizes this defect.
(3) Small changes in hatch spacing does not significantly affect cooling rate and the secondary dendrite arm spacing.
(4) From the calculated values of temperature gradient and growth rate, it is found that columnar dendrites are likely to form during PBF of SS 316. This finding is also consistent with the experimental observation reported in the literature. Rapid scanning and thinner layers enhance cooling rate and micro-hardness but reduce secondary dendrite arm spacing of SS 316 and AlSi10Mg.
(5) The shape of the molten pool is slightly asymmetric except for the first hatch. As the deposition continues, one side of the molten pool interfaces with the already deposited dense metal while the other side is surrounded by the low thermal conductivity powder bed. Asymmetry in the molten pool can be minimized by reducing the scanning speed and increasing packing efficiency.
(6) The first hatch produces larger liquid pool than the other hatches because heat transfer from the liquid pool to its surroundings improves slightly from the first to the subsequent hatches. This is because in the first hatch the liquid pool is surrounded by the powder bed on both sides while in subsequent hatches one side of the liquid pool interfaces with already deposited dense metal. For the upper layers, since heat transfer from the molten pool to the substrate becomes progressively slower, molten pool size increases and cooling rate decreases.

Acknowledgements

We acknowledge the support from the US Department of Energy Nuclear Energy University Program grant number DE-NE0008280. One of the authors acknowledges support of an American Welding Society research fellowship, grant number 179466. We also acknowledge helpful discussions with J.S. Zuback and G.L. Knapp of Penn State University.

Data availability

The raw/processed data required to reproduce these findings cannot be shared at this time due to technical or time limitations.

References

[1] T. DebRoy, H.L. Wei, J.S. Zuback, T. Mukherjee, J.W. Elmer, J.O. Milewski, A.M. Beese, A. Wilson-Heid, A. De, W. Zhang, Additive manufacturing of metallic components – Process, structure and properties, Prog. Mater. Sci. 92 (2018) 112–224.
[2] T. Mukherjee, W. Zhang, T. DebRoy, An improved prediction of residual stresses and distortion in additive manufacturing, Comput. Mater. Sci. 126 (2017) 360–372.
[3] T. Mukherjee, J.S. Zuback, W. Zhang, T. DebRoy, Residual stresses and distortion in additively manufactured compositionally graded and dissimilar joints, Comput. Mater. Sci. 143 (2018) 325–337.
[4] U.S. Bertoli, G. Guss, S. Wu, M.J. Matthews, J.M. Schoenung, In-situ characterization of laser-powder interaction and cooling rates through high-speed imaging of

powder bed fusion additive manufacturing, Mater. Des. 135 (2017) 385–396.
[5] B. Cheng, S. Price, J. Lydon, K. Cooper, K. Chou, On process temperature in powder-bed electron beam additive manufacturing: model development and validation, J Manufac. Sci. Eng. 136 (6) (2014) 061018.
[6] K. Zeng, D. Pal, H.J. Gong, N. Patil, B. Stucker, Comparison of 3DSIM thermal modelling of selective laser melting using new dynamic meshing method to ANSYS, Mater. Sci. Technol. 31 (8) (2015) 945–956.
[7] M. Jamshidinia, R. Kovacevic, The influence of heat accumulation on the surface roughness in powder-bed additive manufacturing, Surf. Topogr.: Metrol. Prop. 3 (1) (2015) 014003.
[8] Q. Shi, D. Gu, M. Xia, S. Cao, T. Rong, Effects of laser processing parameters on thermal behavior and melting/solidification mechanism during selective laser melting of TiC/Inconel 718 composites, Opt. Laser Technol. 84 (2016) 9–22.
[9] I.A. Roberts, C.J. Wang, R. Esterlein, M. Stanford, D.J. Mynors, A three-dimensional finite element analysis of the temperature field during laser melting of metal powders in additive layer manufacturing, Int. J Machine Tool Manufac. 49 (12–13) (2009) 916–923.
[10] Y. Li, K. Zhou, S.B. Tor, C.K. Chua, K.F. Leong, Heat transfer and phase transition in the selective laser melting process, Int. J Heat Mass Trans. 108 (2017) 2408–2416.
[11] R. Andreotta, L. Ladani, W. Brindley, Finite element simulation of laser additive melting and solidification of Inconel 718 with experimentally tested thermal properties, Finite Elem. Anal. Des. 135 (2017) 36–43.
[12] M. Jamshidinia, F. Kong, R. Kovacevic, Numerical modeling of heat distribution in the electron beam melting® of Ti-6Al-4V, J Manufac. Sci. Eng. 135 (6) (2013) 061010.
[13] S. Li, H. Xiao, K. Liu, W. Xiao, Y. Li, X. Han, J. Mazumder, L. Song, Melt-pool motion, temperature variation and dendritic morphology of Inconel 718 during pulsed-and continuous-wave laser additive manufacturing: A comparative study, Mater. Des. 119 (2017) 351–360.
[14] A. Basak, R. Acharya, S. Das, Modeling and characterization of microstructure evolution in single-crystal superalloys processed through scanning laser epitaxy, in: Proc. 26th Annu. Int. Solid Freeform Fabr. Symp. (The University of Texas at Austin, Austin, TX, 2015), 2015, pp. 1237.
[15] D. Dai, D. Gu, Tailoring surface quality through mass and momentum transfer modeling using a volume of fluid method in selective laser melting of TiC/AlSi10Mg powder, Int. J Machine Tool Manufac. 88 (2015) 95–107.
[16] M. Megahed, H.W. Mindt, N. N'Dri, H. Duan, O. Desmaison, Metal additive-manufacturing process and residual stress modeling, Integrate. Mater. Manufac. Innovate. 5 (1) (2016) 4.
[17] Y.S. Lee, W. Zhang, Modeling of heat transfer, fluid flow and solidification microstructure of nickel-base superalloy fabricated by laser powder bed fusion, Additive Manufac. 12 (2016) 178–188.
[18] C. Körner, A. Bauereiß, E. Attar, Fundamental consolidation mechanisms during selective beam melting of powders, Model. Simul. Mater. Sci. Eng. 21 (8) (2013) 085011.
[19] C. Körner, E. Attar, P. Heinl, Mesoscopic simulation of selective beam melting processes, J. Mater. Process. Technol. 211 (6) (2011) 978–987.
[20] M. Xia, D. Gu, G. Yu, D. Dai, H. Chen, Q. Shi, Influence of hatch spacing on heat and mass transfer, thermodynamics and laser processability during additive manufacturing of Inconel 718 alloy, Int. J. Machine Tool Manufac. 109 (2016) 147–157.
[21] A. Bauereiß, T. Scharowsky, C. Körner, Defect generation and propagation mechanism during additive manufacturing by selective beam melting, J. Mater. Process. Technol. 214 (11) (2014) 2522–2528.
[22] S.A. Khairallah, A.T. Anderson, A. Rubenchik, W.E. King, Laser powder-bed fusion additive manufacturing: Physics of complex melt flow and formation mechanisms of pores, spatter, and denudation zones, Acta Mater. 108 (2016) 36–45.
[23] K.C. Mills, Recommended Values of Thermo-Physical Properties for Selected Commercial Alloys, Woodhead Publishing, Cambridge, 2002.
[24] V. Manvatkar, A. De, T. DebRoy, Spatial variation of melt pool geometry, peak temperature and solidification parameters during laser assisted additive manufacturing process, Mater. Sci. Technol. 31 (2015) 924–930.
[25] T. Mukherjee, J.S. Zuback, A. De, T. DebRoy, Printability of alloys for additive manufacturing, Sci. Rep. 6 (2016).
[26] V. Manvatkar, A. De, T. DebRoy, Heat transfer and material flow during laser assisted multi-layer additive manufacturing, J. Appl. Phys. 116 (12) (2014) 124905.
[27] T. DebRoy, S.A. David, Physical processes in fusion welding, Rev. Mod. Phys. 67 (1) (1995) 85.
[28] A. Foroozmehr, M. Badrossamay, E. Foroozmehr, S. Golabi, Finite element simulation of selective laser melting process considering optical penetration depth of laser in powder bed, Mater. Des. 89 (2016) 255–263.
[29] Y.C. Wu, W.S. Hwang, C.H. San, C.H. Chang, H.J. Lin, Parametric study of surface morphology for selective laser melting on Ti6Al4V powder bed with numerical and experimental methods, Int. J. Mater. Form. (2017), http://dx.doi.org/10.1007/s12289-017-1391-2.
[30] T. DebRoy, W. Zhang, J. Turner, S.S. Babu, Building digital twins of 3D printing machines, Scr. Mater. 134 (2017) 61–65.
[31] T. Craeghs, S. Clijsters, E. Yasa, F. Bechmann, S. Berumen, J.P. Kruth, Determination of geometrical factors in layerwise laser melting using optical process monitoring, Opt. Laser Eng. 49 (12) (2011) 1440–1446.
[32] S. Kou, Welding Metallurgy, 2nd ed., Wiley, Hoboken, New Jersey, 2003.
[33] T. Mukherjee, V. Manvatkar, A. De, T. DebRoy, Dimensionless numbers in additive manufacturing, J Appl. Phys. 121 (6) (2017) 064904.
[34] G.L. Knapp, T. Mukherjee, J.S. Zuback, H.L. Wei, T.A. Palmer, A. De, T. DebRoy, Building blocks for a digital twin of additive manufacturing, Acta Mater. 135 (2017) 390–399.
[35] M. Tang, P. Chris Pistorius, S. Narra, J.L. Beuth, Rapid solidification: selective laser melting of AlSi10Mg, JOM 68 (3) (2016) 960–966.
[36] K.G. Prashanth, S. Scudino, H.J. Klauss, K.B. Surreddi, L. Löber, Z. Wang, A.K. Chaubey, U. Kühn, J. Eckert, Microstructure and mechanical properties of Al–12Si produced by selective laser melting: Effect of heat treatment, Mater. Sci. Eng. A 590 (2014) 153–160.
[37] K. Zhang, S. Wang, W. Liu, X. Shang, Characterization of stainless steel parts by laser metal deposition shaping, Mater. Des. 55 (2014) 104–119.
[38] M. Ma, Z. Wang, X. Zeng, A comparison on metallurgical behaviors of 316L stainless steel by selective laser melting and laser cladding deposition, Mater. Sci. Eng.: A 685 (2017) 265–273.
[39] A.A. Raus, M.S. Wahab, M. Ibrahim, K. Kamarudin, A. Ahmed, S. Shamsudin, Mechanical and physical properties of AlSi10Mg processed through selective laser melting, AIP Conf. Proc. 1831 (1) (2017) 020027.
[40] H.D. Carlton, A. Haboub, G.F. Gallegos, D.Y. Parkinson, A.A. MacDowell, Damage evolution and failure mechanisms in additively manufactured stainless steel, Mater. Sci. Eng. A 651 (2016) 406–414.
[41] T. Mukherjee, V. Manvatkar, A. De, T. DebRoy, Mitigation of thermal distortion during additive manufacturing, Scr. Mater. 127 (2017) 79–83.